Dynamic Thermal Emission Control Based on Ultrathin Plasmonic Metamaterials Including Phase-Changing Material GST

Yurui Qu, Qiang Li, Kaikai Du, Lu Cai, Jun Lu, and Min Qiu*

Dynamic thermal emission control has attracted growing interest in a broad range of fields, including radiative cooling, thermophotovoltaics and adaptive camouflage. Previous demonstrations of dynamic thermal emission control present disadvantages of either large thickness or requiring sustained electrical or thermal excitations. In this paper, an ultrathin (~0.023λ, λ is the emission peak wavelength) metal-insulator-metal plasmonic metamaterial-based zero-static-power mid-infrared thermal emitter incorporating phase-changing material GST is experimentally demonstrated to dynamically control the thermal emission. The electromagnetic modes can be continuously tuned through the intermediate phases determined by controlling the temperature. A typical resonance mode, which involves the coupling between the high-order magnetic resonance and anti-reflection resonance, shifts from 6.51 to 9.33 μm while GST is tuned from amorphous to crystalline phase. This demonstration will pave the way towards the dynamical thermal emission control in both the fundamental science field and a number of energy-harvesting applications.

1. Introduction

The ability to control thermal emission contributes to a wide range of applications including radiative cooling,[1–3] thermophotovoltaics,[4–10] and adaptive camouflage.[11–13] Plasmonic nanostructures have unique potentials in the control of thermal emission. Thanks to high resonance-enhanced Joule loss in plasmonic nanostructures, they have strong absorption that can be engineered by smart geometric designs and thereby can be used to control thermal emission according to Kirchhoff's law. To date, several plasmonic nanostructures have been used to statically control thermal emission including gratings,[14–16] metal-insulator-metal (MIM) structures,[17–27] metallic bull's eye.[28,29] Such plasmonic nanostructure-based thermal emitters are ultrathin because metallic nanostructures can effectively concentrate light into nanoscale and thermal radiation thereby occurs in a size smaller than the free-space wavelength of radiation. However, they can only offer a static thermal emission control without flexible tunability.

Several strategies to dynamically engineer thermal emission have also been investigated. (1) By electrically tuning intersubband absorption in quantum wells and carrier density in graphene, the emissivities of mid-infrared thermal emitters based on photonic crystal slabs[30] and graphene resonators[31] can be dynamically tailored, respectively. For the photonic-crystal-slab-based thermal emitter, the peak emission wavelength based on an intersubband transition is untunable because two quantized energy levels in the conduction band of quantum wells are fixed. The thickness of the photonic-crystal slab-based thermal emitter is as large as 2 μm (~0.2λ, λ is the emission peak wavelength). For the graphene-resonator-based emitter, the emissivity can only be tuned in a small range from 0 to 3% when carrier density increases from 0.1×10^{13} cm^{-2} to 1.2×10^{13} cm^{-2}. (2) By mechanically controlling the distance between the top metamaterial pattern and the bottom metallic film through applying heat, the thermal emission in micro-electro-mechanical systems can be tunable.[32] It is difficult to tune the peak wavelength in such structures, and the emissivity can only be tuned in a limited range from 50% to 80% when the temperature increases from 293 K to 623 K. The thickness of the whole structure is as large as 2 μm (~0.4λ) in order to suspend top metamaterial pattern above the ground plane. (3) By thermally controlling the phases of phase-changing materials like Ge2Sb2Te5 (GST)[33] and VOx[34] at different temperatures, tunable thermal emission can be realized based on multilayer structures. The peak wavelength tuning is dependent on the thickness of GST or VOx and the thermal emitters thus present comparatively low design flexibility. In addition, the VOx is volatile and thus requires sustained power to maintain its phases, which leads to large power consumption. There has yet to emerge a viable solution to realize ultrathin thermal emitters with dynamic low-power-consumption thermal emission control.

In this paper, an ultrathin plasmonic thermal emitter is experimentally demonstrated to dynamically control thermal emission

Y. Qu, Q. Li, K. Du, L. Cai, J. Lu, M. Qiu
State Key Laboratory of Modern Optical Instrumentation
College of Optical Science and Engineering
Zhejiang University
Hangzhou, 310027, China
E-mail: qiangli@zju.edu.cn

The ORCID identification number(s) for the author(s) of this article can be found under https://doi.org/10.1002/lpor.201700091

DOI: 10.1002/lpor.201700091

with low-power-consumption. The ultrathin feature is achieved by adopting the MIM plasmonic metamateirals, in which the emission wavelength can be controlled by the geometric size of top metallic particles without sacrificing the total device thickness. The dynamic low-power-consumption control is implemented by incorporating zero-static-power phase-changing material Ge2Sb2Te5 (GST), which has been applied in various energy-efficient switchable photonic devices.[33,35–44] The whole structure shows a total thickness of 550 nm (~0.023λ), which is well below the subwavelength scale. A typical resonance mode, which involves the coupling between the high-order magnetic resonance and anti-reflection resonance, shifts from 6.51 to 9.33 μm while GST is tuned from amorphous to crystalline phase. This ultrathin plasmonic nanostructure combined with zero-static-power phase-changing material paves a new way to dynamically control thermal emission.

2. Materials and Methods

2.1. Fabrication of GST-Based Thermal Emitter

A 100-nm-thick Au film and subsequently a 350 nm GST film are deposited on silicon substrate by magnetron sputtering. A 1.5-μm-thick photoresist (AR-P 5350) is then spun onto the GST film and baked for 5 minutes at 105 °C. The photoresist is exposed to define the nanohole array by photolithography using Double Sided Mask Aligner System (MA6–BSA). The photoresist is then developed in 1:6 AR 300–26/ DI water followed by rinsing in DI water. After development, a 100-nm-thick Au film is then deposited onto the sample by magnetron sputtering. The Au absorber is realized after lift-off by ultrasonic processing in acetone for 1 minute.

2.2. Optical Measurements

The emitted spectra are measured by a Fourier transform infrared spectrometer (FTIR) with a room-temperature doped triglycine sulfate (DTGS) detector. The black soot is generally regarded as a perfect reference owing to its high wavelength-independent emissivity. Here the black soot reference is made by firing a rectangular stainless steel slice with a candle and its emissivity is assumed to be 0.97. The as-deposited GST alloy is at the amorphous phase and an annealing process at 160°C on a hot plate is applied to get the crystalline GST in this paper. The thermal emitter is fixed on a heating stage with a temperature range of 0–300°C. The baking temperature is read out from heating stage display, which is around 9°C higher than temperature of the sample surface measured by a thermocouple. In the following experimental results, temperature refers to baking temperature.

2.3. Numerical Simulations

Finite-difference time-domain method (FDTD Solutions v8.13, Lumerical) is used to compute the optical responses of the MIM thermal emitter. The relative permittivity of gold is obtained from Palik's handbook.[45] The relative permittivities of GST (2.5-15 μm) are obtained experimentally from the fabricated GST films (Fig. S1), and the permittivities used in simulation (2.5-25 μm) are obtained by fitting experimental permittivities based on multi-coefficient models (MCMs) in FDTD Solutions. According to Kirchhoff's law of thermal radiation, the thermal emissivity of the sample is equal to its absorptivity, so the simulated emissivity is replaced by the simulated absorptivity. All of the simulated results are obtained under the normal incidence.

3. Results and Discussion

3.1. Thermal Emissivities of aGST and cGST MIM Thermal Emitter

The schematic of the tunable ultrathin MIM plasmonic thermal emitter is depicted in **Figure 1**(a), and Figure 1b presents corresponding scanning electron microscope (SEM) images. The thicknesses of the bottom gold film, the intermediate GST film and the top gold nanodisks of the fabricated MIM thermal emitter are 100 nm, 350 nm and 100 nm, respectively. The total thickness is 550 nm, which equals to around 0.023λ (λ is 23.78 μm for the fundamental magnetic resonance). The array periodicity is 5 μm, and the diameter of the nanodisks is 2.8 μm. The total dimension of the nanostructure arrays is 9 × 9 mm^2. The as-deposited GST is at the amorphous phase (termed as aGST). An annealing process above 160°C on a hot plate is applied to get GST at the crystalline phase (termed as cGST) (inset in Figure 1(a)). The experimental and simulated emissivities are obtained at normal incidence. The electric field E, the magnetic field H and the wave vector k are at x, y and z directions, respectively, as shown in Figure 1(a).

The emissivities of the MIM thermal emitter at normal incidence are investigated in experiments (**Figure 2**(a)) and simulations (Figure 2(b)). For the aGST MIM emitter, several resonant emission peaks can be seen in the experimental emissivity spectrum. The emission peaks at 23.78 μm with an emissivity of 0.70 and 8.66 μm with an emissivity of 0.70 correspond to the fundamental magnetic resonance (the magnetic field pattern is shown in the inset of Figure 2(b)) and the third-order magnetic resonance, respectively. There are two overlapping resonances peaking at 6.26 μm and 5.85 μm, respectively. Both peaks have the emissivity of around 0.9. For the cGST MIM emitter, only one broad emission peak locating at 8.71 μm with an emissivity of 0.73 can be identified (Figure 2(a)). The spectral range of the DTGS detector used in this experiment is 2.5-25 μm, and the fundamental magnetic resonance shift beyond this range when GST is tuned from amorphous to crystalline phase. Therefore, in the following analysis of the emission evolution process, we focus on other resonant modes. The measured peak emissivities are generally lower than the simulated ones for both aGST and cGST thermal emitters, especially for the long wavelength (> 7 μm). This may be caused by the rough disk boundaries owing to the imperfection in fabrication and the error in fitting experimental permittivities based on multi-coefficient models (MCMs).

3.2. Mode Analysis

To unveil the physics behind the different peaks of the aGST MIM emitter, the field patterns for the aGST MIM emitter are

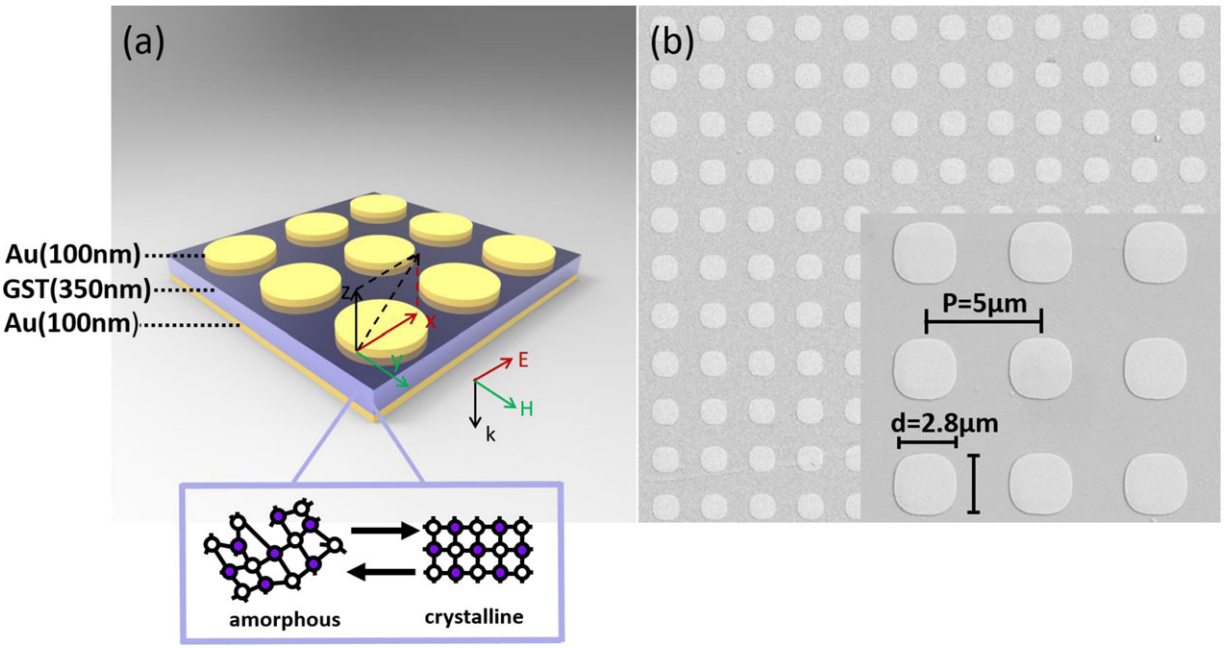

Figure 1. (a) A schematic of and (b) an SEM image of the fabricated ultrathin MIM plasmonic thermal emitter incorporating phase-changing material GST. The MIM thermal emitter is composed of the bottom gold film, the intermediate GST film and the top nanodisks. Inset: amorphous to crystalline phase transition for the phase-changing material GST.

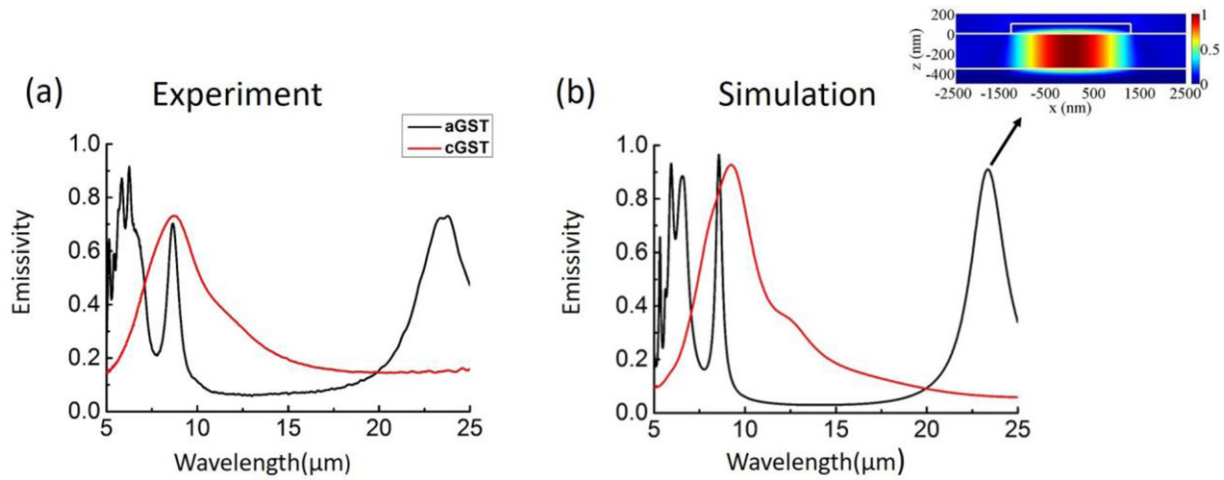

Figure 2. (a) and (b) are experimental and simulated thermal emissivities of the MIM thermal emitter. The black and red lines are for the aGST and cGST phases, respectively. Inset: The field pattern of the fundamental magnetic resonance. The colormap represents the amplitude of magnetic field.

further investigated (**Figure 3**). The simulated emissivity of the aGST MIM emitter is fitted by multiple Lorenz curves. The fitting Lorenz function is $L(x) = L_0 + \frac{A_0}{\pi}\frac{\frac{1}{2}\Gamma}{(\lambda-\lambda_0)^2+(\frac{1}{2}\Gamma)^2}$. It has the maximum at $\lambda = \lambda_0$ and Γ denotes the full width at half maximum (FWHM).

The emissivity of the aGST MIM emitter is fitted by four Lorenz curves, representing four main resonant modes (Mode I to Mode IV). The peak wavelengths of four resonant modes are 8.70 μm, 6.51 μm, 5.86 μm and 5.28 μm, indicated by A, B, C and D (Figure 3), respectively. The four colormaps represent the magnetic field component Hy, which is perpendicular to cross section xz at the corresponding peak wavelength. There is a good agreement between the black curve which represents the simulated emissivity, and the pink curve which represents the cumulative fitting curves of the four main resonant modes.

The magnetic field of Mode I is confined to the intermediate GST film between the top Au nanodisks and bottom Au layers, signifying that a typical three-order magnetic resonance is generated. The magnetic fields of Mode II, Mode III and Mode IV are not only confined to the intermediate GST film between the Au top nanodisks and bottom layers, but also in the interface between the GST film and the bottom film (known as

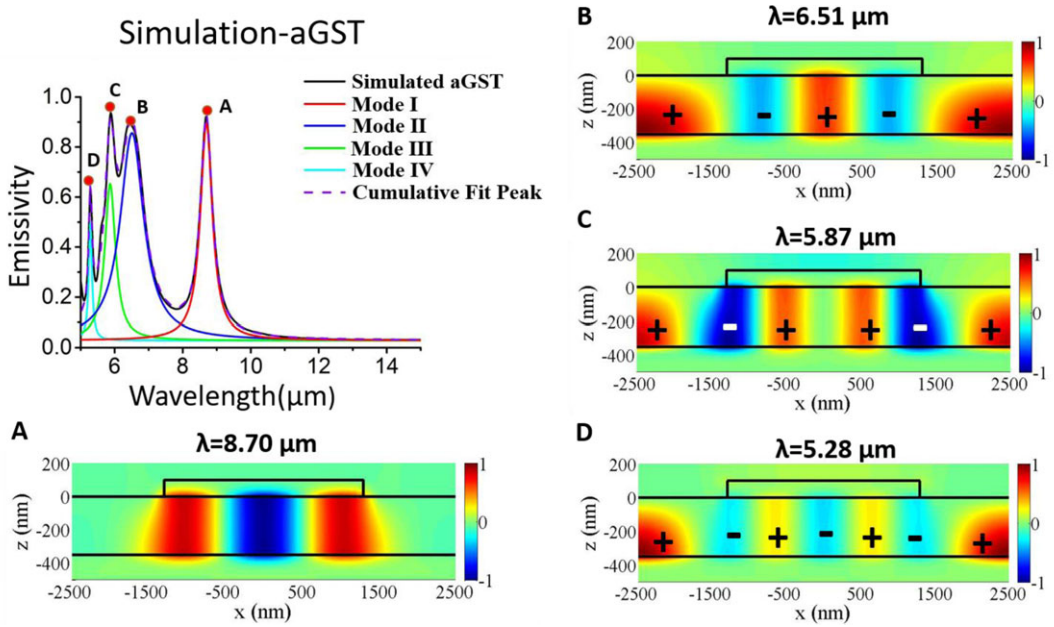

Figure 3. Multiple Lorenz fitting of the simulated aGST MIM emitter emissivity. A-D represent the peak wavelength of different resonant modes of the aGST MIM emitter. The colormaps represent the magnetic field component Hy. The positive Hy is represented by the plus sign (+), and the negative Hy is represented by the minus sign (−).

anti-reflection resonance). These three peaks (B, C and D) correspond to the hybrid modes which involve the coupling between the high-order magnetic resonances and anti-reflection resonances between the GST film and the Au bottom film. Magnetic field components (Hy) of four resonance modes are symmetric with respect to x = 0 plane at normal incidence.

3.3. Evolution of the Modes through the Intermediate Phases

The crystallization temperature of GST is around 160°C. In order to explore evolution of the different resonant modes through the intermediate phases, The MIM thermal emitter is baked at 1°C step from 160°C to 175°C to get different GST intermediate phases. The baking time is 1 min for each temperature, and temperature rising time is 20s and another 40s is for emission spectrum measurement. The emissivities of the MIM thermal emitter are measured at corresponding baking temperatures. In **Figure 4**(a), the emissivities of the MIM emitter at several intermediate GST phases are represented. As temperature increases, many GST crystalline nuclei are formed at first and then numerous crystals gradually joint together to form the crystalline structure at crystallization temperature. The GST film in the intermediate phases consists of different proportions of amorphous and crystalline molecules, and the effective permittivity $\varepsilon_{eff}\lambda$ of such GST film can be estimated by effective-medium theories[47] based on the Lorentz-Lorenz relation[40,46,48]:

$$\frac{\varepsilon_{eff}(\lambda)-1}{\varepsilon_{eff}(\lambda)+2} = m \times \frac{\varepsilon_c(\lambda)-1}{\varepsilon_c(\lambda)+2} + (1-m) \times \frac{\varepsilon_a(\lambda)-1}{\varepsilon_a(\lambda)+2}$$

m denotes the crystallization fraction of the GST film ranging from 0 to 100%, $\varepsilon_c(\lambda)$ and $\varepsilon_a(\lambda)$ are the permittivities of GST in the crystalline and amorphous phases. Simulated resonances are matched with the measured resonances by changing the crystallization fraction of GST from 0% to 100%.

The simulated emissivities at intermediate phases are fitted by multiple Lorenz curves to explore the evolution of each resonant mode. In Figure 4(b), all the four resonant modes red-shift as temperature grows, indicating that the real part of the refractive index of the GST spacer film increases. When the GST film is fully crystallized (crystallization fraction from 0% to 100%), the Mode I redshifts from 8.70 μm to 12.78 μm. The Mode II and III shift from 6.51 μm to 9.33 μm and from 5.87 μm to 7.93 μm, respectively. The Mode IV redshifts from 5.28 μm to 6.05 μm when the crystallization fraction increases from 0% to 50%, and vanishes at crystallization fraction of 70%. The bandwidths and emissivities for each resonant mode at different crystallization fractions are extracted from Lorenz fitting curves (Figure 4(c) and (d)). The bandwidths of all four resonant modes increase as GST crystallization fraction grows (Figure 4(c)) because the GST gets more lossy at higher crystallization fraction (Figure S2). Specially, the bandwidth of Mode 1 increases sharply after the crystallization fraction of 70%. The emissivities of Mode I, Mode III and Mode IV decrease as crystallization fraction grows. With crystallization fraction increasing, the emissivity of Mode II slightly increases first and then gradually decreases. The Mode II is the resonant mode with non-optimal coupling at aGST phase, and goes through the optimal coupling with the highest emissivity at 30% crystallization. The emissivity then decreases with crystallization fraction increasing from 30% to 100%.

The reamorphization of GST can be achieved by thermal annealing at a temperature above 640°C followed by a sharp cooling, and the phase transition process takes several seconds. The reamorphization is not demonstrated here because the 100-nm-thick Au film exhibits a melting point of around 300°C. If

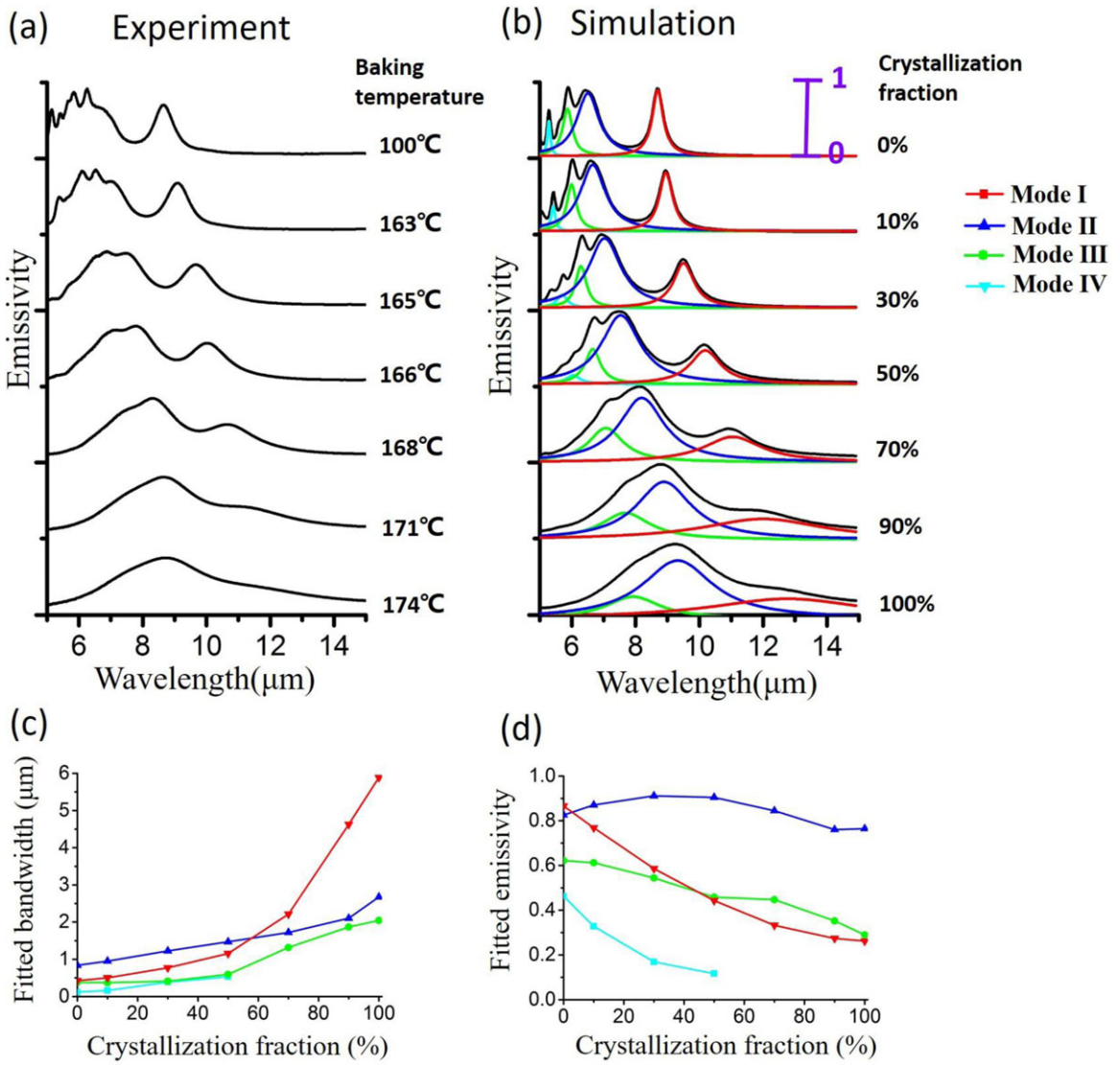

Figure 4. Evolution of different resonant modes through the intermediate phases. (a) Experimental results of continuously tuning emissivities of the MIM thermal emitter at different baking temperatures. (b) Simulated emissivities of the MIM thermal emitter at corresponding crystallization fraction. The simulated emissivities at intermediate phases are fitted by multiple Lorenz curves. Extracted (c) bandwidths and (d) emissivities of the four resonant modes versus crystallization fraction.

the gold is replaced by refractory metals (such as W and Mo), the GST-based MIM thermal emitter can be reversibly switchable. In addition to thermal annealing, the reamorphization of the GST can also be realized using laser pulses[35,38,49–51] or electrical stimulations.[52] The typical switching time for electrical stimulation is several nanoseconds.[52] By using laser pulses, the switching time can be several nanoseconds[35] or even reduced to tens of femtoseconds.[50]

4. Conclusions and Outlook

In conclusion, an ultrathin plasmonic thermal emitter with dynamic thermal emission control ability is experimentally investigated. The ultrathin thermal emitter has the thickness of 550 nm (~0.023λ), which is well below the subwavelength scale. The dynamic zero-static-power control is achieved by incorporating phase-changing material GST. The emissivities, bandwidths and peak wavelengths can be continuously tuned by controlling the temperature that determines the crystallization fraction of GST. Except for the thermally tunable GST, the phase transitions of GST can also be induced by electrical[37,52] or optical excitation,[35,38,42,49–51] demonstrating potentials in ultrafast modulation of GST based matematerials. This ultrathin plasmonic metamaterials-based thermal emitter paves the way towards the dynamic thermal emission control in fundamental science and can significantly benefit a number of applications, including radiative cooling, thermophotovoltaics and adaptive camouflage.

Supporting Information

Supporting Information is available from the Wiley Online Library or from the author.

Acknowledgements

The authors would like to thank Yuanqing Yang at University of Southern Denmark for helpful discussion. This work is supported by the National Key Research and Development Program of China (Grant No. 2017YFA0205700) and National Natural Science Foundation of China (Grant Nos. 61425023, 61575177 and 61235007).

Conflict of Interest

The authors have declared no conflict of interest.

Keywords

thermal emitter, phase-changing material GST, dynamic, ultrathin, plasmonic

Received: April 12, 2017
Revised: July 24, 2017
Published online: August 29, 2017

[1] A. P. Raman, M. A. Anoma, L. Zhu, E. Rephaeli, S. Fan, *Nature* **515**, 540–544 (2014).
[2] P. Hsu, A. Y. Song, P. B. Catrysse, C. Liu, Y. Peng, J. Xie, S. Fan, Y. Cui, *Science* **353**, 1019–1023 (2016).
[3] Y. Zhai, Y. Ma, S. N. David, D. Zhao, R. Lou, G. Tan, R. Yang, X. Yin, *Science* **355**, 1062–1066 (2017).
[4] P. Nagpal, S. E. Han, A. Stein, D. J. Norris, *Nano Lett.* **8**, 3238–3243 (2008).
[5] E. Rephaeli, S. Fan, *Opt. Exp.* **17**, 15145–15159 (2009).
[6] W. R. Chan, P. Bermel, R. C. N. Pilawa-Podgurski, C. H. Marton, K. F. Jensen, J. J. Senkevich, J. D. Joannopoulos, M. Soljacic, I. Celanovic, *Proceedings of the National Academy of Sciences* **110**, 5309–5314 (2013).
[7] A. Lenert, D. M. Bierman, Y. Nam, W. R. Chan, I. Celanović, M. Soljačić, E. N. Wang, *Nature Nanotechnol.* **9**, 126–130 (2014).
[8] P. N. Dyachenko, S. Molesky, A. Y. Petrov, M. Stormer, T. Krekeler, S. Lang, M. Ritter, Z. Jacob, M. Eich, *Nat. Commun.* **7**, 11809 (2016).
[9] T. Asano, M. Suemitsu, K. Hashimoto, M. D. Zoysa, T. Shibahara, T. Tsutsumi, S. Noda, *Sci. Adv.* **2**, e1600499 (2016).
[10] J. Zhou, X. Chen, L. J. Guo, *Adv. Mater.* **28**, 3017–3023 (2016).
[11] A. Pohl, J. Fagerström, H. Kariis, R. Lindell, T. Hallberg, H. Högström, *SPIE Security+ Defence. International Society for Optics and Photonics* 99970C–99970C (2016)
[12] C. Yu, Y. Li, X. Zhang, X. Huang, V. Malyarchuk, S. Wang, Y. Shi, L. Gao, Y. Su, Y. Zhang, H. Xu, R. T. Hanlon, Y. Huang, J. A. Rogers, *Proceedings of the National Academy of Sciences* **111**, 12998–13003 (2014).
[13] L. Xiao, H. Ma, J. Liu, W. Zhao, Y. Jia, Q. Zhao, K. Liu, Y. Wu, Y. Wei, S. Fan, K. Jiang, *Nano Lett.* **15**, 8365–8370 (2015).
[14] J. J. Greffet, R. Carminati, K. Joulain, J. P. Mulet, S. P. Mainguy, Y. Chen, *Nature* **416**, 61–64 (2002).
[15] H. T. Miyazaki, K. Ikeda, T. Kasaya, K. Yamamoto, Y. Inoue, K. Fujimura, T. Kanakugi, M. Okada, K. Hatade, S. Kitagawa, *Appl. Phys. Lett.* **92**, 141114 (2008).
[16] J. Liu, U. Guler, A. Lagutchev, A. Kildishev, O. Malis, A. Boltasseva, V. M. Shalaev, *Opt. Mater. Express.* **5**, 2721 (2015).
[17] M. Diem, T. Koschny, C. M. Soukoulis, *Phys. Rev B* **79**, 033101 (2009).
[18] J. Mason, D. Wasserman, S. Smith, *Appl. Phys. Lett.* **98**, 241105 (2011).
[19] X. Liu, T. Tyler, T. Starr, A. F. Starr, N. M. Jokerst, W. J. Padilla, *Phys. Rev. Lett.* **107**, 045901 (2011).
[20] C. Arnold, F. O. Marquier, M. Garin, F. Pardo, S. Collin, N. Bardou, J. Pelouard, J. Greffet, *Phys. Rev B* **86**, 035316 (2012).
[21] H. T. Miyazaki, T. Kasaya, M. Iwanaga, B. Choi, Y. Sugimoto, K. Sakoda, *Appl. Phys. Lett.* **105**, 121107 (2014).
[22] D. Costantini, A. Lefebvre, A. L. Coutrot, I. Moldovan-Doyen, J. P. Hugonin, S. Boutami, F. Marquier, H. Benisty, J. J. Greffet, *Phys. Rev. Appl.* **4**, 014023 (2015).
[23] M. Makhsiyan, P. Bouchon, J. Jaeck, J. Pelouard, R. Haïdar, *Appl. Phys. Lett.* **107**, 251103 (2015).
[24] C. Wang, D. P. Tsai, *Opt. Express* **24**, 18382 (2016).
[25] C. Y. Liao, C. Wang, B. H. Cheng, Y. Chen, W. Tsai, D. Feng, T. Yeh, T. Yen, D. P. Tsai, *Appl. Phys. Lett.* **109**, 261101 (2016).
[26] X. Zhang, H. Liu, Z. G. Zhang, Q. Wang, S. N. Zhu, *Sci. Rep.* **7**, 41858 (2017).
[27] B. Liu, W. Gong, B. Yu, P. Li, S. Shen, *Nano. Lett.* **17**, 666–672 (2017).
[28] S. E. Han, D. J. Norris, *Opt. Express* **18**, 4829–4837 (2010).
[29] J. H. Park, S. E. Han, P. Nagpal, J. G. Tischler, D. J. Norris, *ACS Photonics* **3**, 494 (2016).
[30] T. Inoue, M. D. Zoysa, T. Asano, S. Noda, *Nat. Mater.* **13**, 928–931 (2014).
[31] V. W. Brar, M. C. Sherrott, M. S. Jang, S. Kim, L. Kim, M. Choi, L. A. Sweatlock, H. A. Atwater, *Nat. Commun.* **6**, 7032 (2015).
[32] X. Liu, W. J. Padilla, *Adv. Mater.* **28**, 871–875 (2016).
[33] K. Du, Q. Li, Y. Lyu, J. Ding, Y. Lu, Z. Cheng, M. Qiu. *Light: Science & Applications* **6**, e16194 (2017).
[34] M. A. Kats, R. Blanchard, S. Zhang, P. Genevet, C. Ko, S. Ramanathan, F. Capasso, *Phys. Rev. X* **3**, 041004 (2013).
[35] B. Gholipour, J. Zhang, K. F. MacDonald, D. W. Hewak, N. I. Zheludev, *Adv. Mater.* **25**, 3050–3054 (2013).
[36] P. Hosseini, C. D. Wright, H. Bhaskaran, *Nature* **511**, 206–211 (2014).
[37] F. F. Schlich, P. Zalden, A. M. Lindenberg, R. Spolenak, *ACS Photonics* **2**, 178–182 (2015).
[38] C. Ríos, M. Stegmaier, P. Hosseini, D. Wang, T. Scherer, C. D. Wright, H. Bhaskaran, W. H. P. Pernice, *Nat. Photonics* **9**, 725–732 (2015).
[39] Q. Wang, E. T. F. Rogers, B. Gholipour, C. Wang, G. Yuan, J. Teng, N. I. Zheludev, *Nat. Photonics* **10**, 60–65 (2015).
[40] C. H. Chu, M. L. Tseng, J. Chen, P. C. Wu, Y. Chen, H. Wang, T. Chen, W. T. Hsieh, H. J. Wu, G. Sun, D. P. Tsai, *Laser Photonics Rev.* **10**, 986–994 (2016).
[41] S. Yoo, T. Gwon, T. Eom, S. Kim, C. S. Hwang, *ACS Photonics* **3**, 1265–1270 (2016).
[42] P. Li, X. Yang, T. W. W. Maß, J. Hanss, M. Lewin, A. U. Michel, M. Wuttig, T. Taubner, *Nat. Mater.* **15**, 870–875 (2016).
[43] M. Rudé, V. Mkhitaryan, A. E. Cetin, T. A. Miller, A. Carrilero, S. Wall, F. J. G. de Abajo, H. Altug, V. Pruneri, *Adv. Opt. Mater.* **4**, 1060–1066 (2016).
[44] A. Tittl, A. U. Michel, M. Schäferling, X. Yin, B. Gholipour, L. Cui, M. Wuttig, T. Taubner, F. Neubrech, H. Giessen, *Adv. Mater.* **27**, 4597–4603 (2015)
[45] E. D. Palik, *Handbook of optical constants of solids* (Vol. **3**. Academic press, 1998), pp. 290–295.
[46] Y. G. Chen, T. S. Kao, B. Ng, X. Li, X. G. Luo, B. Luk'Yanchuk, S. A. Maier, M. H. Hong, *Opt. Exp.* **21**, 13691 (2013).
[47] N. V. Voshchinnikov, G. Videen, T. Henning. *Appl. Opt.* **46**, 4065–4072 (2007).
[48] D. E. Aspnes, *Am. J. Phys.* **50**, 704–709 (1982).
[49] T. Hira, T. Homma, T. Uchiyama, K. Kuwamura, Y. Kihara, T. Saiki, *Appl. Phys. Lett.* **106**, 031105 (2015).
[50] A. K. U. Michel, P. Zalden, D. N. Chigrin, M. Wuttig, A. M. Lindenberg, T. Taubner, *ACS Photonics* **1**, 833–839 (2014).
[51] C. Rios, P. Hosseini, C. D. Wright, H. Bhaskaran, W. H. P. Pernice, *Adv Mater* **26**, 1372–1377 (2014).
[52] Y. Hu, H. Zou, J. Zhang, J. Xue, Y. Sui, W. Wu, L. Yuan, X. Zhu, S. Song, Z. Song, *Appl. Phys. Lett.* **107**, 263105 (2015).

